27. PARTICLE DETECTORS

Revised 2001 (see the various sections for authors).

In this section we give various parameters for common detector components. The quoted numbers are usually based on typical devices, and should be regarded only as rough approximations for new designs. A more detailed discussion of detectors can be found in Ref. 1. In Table 27.1 are given typical spatial and temporal resolutions of common detectors.

Table 27.1: Typical spatial and temporal resolutions of common detectors.

Detector Type	Accuracy (rms)	Resolution Time	Dead Time
Bubble chamber	10 to 150 μm	1 ms	50 ms[a]
Streamer chamber	300 μm	2 μs	100 ms
Proportional chamber	$\geq$ 300 μm[b,c]	50 ns	200 ns
Drift chamber	50 to 300 μm	2 ns[d]	100 ns
Scintillator	—	150 ps	10 ns
Emulsion	1 μm	—	—
Silicon strip	$\frac{\text{pitch}}{3 \text{ to } 7}$ [e]	[f]	[f]
Silicon pixel	2 μm[g]	[f]	[f]

[a] Multiple pulsing time.

[b] 300 μm is for 1 mm pitch.

[c] Delay line cathode readout can give $\pm$150 μm parallel to anode wire.

[d] For two chambers.

[e] The highest resolution ("7") is obtained for small-pitch detectors ($\lesssim$25 μm) with pulse-height-weighted center finding.

[f] Limited at present by properties of the readout electronics. (Time resolution of $\leq$ 25 ns is planned for the ATLAS SCT.)

[g] Analog readout of 34 μm pitch, monolithic pixel detectors.

27.1. Organic scintillators

Revised September 2001 by K.F. Johnson (FSU).

Organic scintillators are broadly classed into three types, crystalline, liquid, and plastic, all of which utilize the ionization produced by charged particles (see the section on "Passage of particles through matter" (Sec. 26.2) of this *Review*) to generate optical photons, usually in the blue to green wavelength regions [2]. Plastic scintillators are by far the most widely used and we address them primarily; however, most of the discussion will

also have validity for liquid scintillators with obvious caveats. Crystal organic scintillators are practically unused in high-energy physics.

Densities range from 1.03 to 1.20 g cm^{-3}. Typical photon yields are about 1 photon per 100 eV of energy deposit [3]. A one-cm-thick scintillator traversed by a minimum-ionizing particle will therefore yield $\approx 2 \times 10^4$ photons. The resulting photoelectron signal will depend on the collection and transport efficiency of the optical package and the quantum efficiency of the photodetector.

Plastic scintillators do not respond linearly to the ionization density. Very dense ionization columns emit less light than expected on the basis of dE/dx for minimum-ionizing particles. A widely used semi-empirical model by Birks' posits that recombination and quenching effects between the excited molecules reduce the light yield [4]. These effects are more pronounced the greater the density of the excited molecules. Birks' formula is

$$\frac{d\mathscr{L}}{dx} = \mathscr{L}_0 \frac{dE/dx}{1 + k_B\, dE/dx} \ , \tag{27.1}$$

where $\mathscr{L}$ is the luminescence, $\mathscr{L}_0$ is the luminescence at low specific ionization density, and k_B is Birks' constant, which must be determined for each scintillator by measurement.

Decay times are in the ns range; rise times are much faster. The combination of high light yield and fast response time allows the possibility of sub-ns timing resolution [5]. The fraction of light emitted during the decay "tail" can depend on the exciting particle. This allows pulse shape discrimination as a technique to carry out particle identification. Because of the hydrogen content (carbon to hydrogen ratio ≈ 1) plastic scintillator is sensitive to proton recoils from neutrons. Ease of fabrication into desired shapes and low cost has made plastic scintillators a common detector component. Recently, plastic scintillators in the form of scintillating fibers have found widespread use in tracking and calorimetry [6].

27.1.1. ***Scintillation mechanism*** :
Scintillation: A charged particle traversing matter leaves behind it a wake of excited molecules. Certain types of molecules, however, will release a small fraction ($\approx 3\%$) of this energy as optical photons. This process, scintillation, is especially marked in those organic substances which contain aromatic rings, such as polystyrene, polyvinyltoluene, and napthalene. Liquids which scintillate include toluene and xylene.

Fluorescence: In fluorescence, the initial excitation takes place via the absorption of a photon, and de-excitation by emission of a longer wavelength photon. Fluors are used as "waveshifters" to shift scintillation light to a more convenient wavelength. Occurring in complex molecules, the absorption and emission are spread out over a wide band of photon energies, and have some overlap, that is, there is some fraction of the emitted light which can be re-absorbed [7]. This "self-absorption" is undesirable for detector applications because it causes a shortened attenuation length. The wavelength difference between the major absorption and emission peaks is called the Stokes' shift. It is usually the case that the greater the Stokes' shift, the smaller the self absorption—thus, a large Stokes' shift is a desirable property for a fluor.

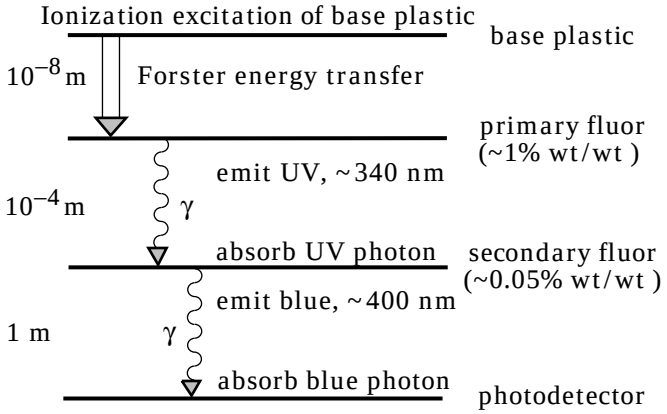

Figure 27.1: Cartoon of scintillation "ladder" depicting the operating mechanism of plastic scintillator. Approximate fluor concentrations and energy transfer distances for the separate sub-processes are shown.

Scintillators: The plastic scintillators used in high-energy physics are binary or ternary solutions of selected fluors in a plastic base containing aromatic rings. (See the appendix in Ref. 8 for a comprehensive list of plastic scintillator components.) Virtually all plastic scintillators contain as a base either polyvinyltoluene, polystyrene, or acrylic, whereby polyvinyltoluene-based scintillator can be up to 50% brighter than the others. Acrylic is non-aromatic and has therefore a very low scintillation efficiency. It becomes an acceptable scintillator when napthalene, a highly aromatic compound, is dissolved into the acrylic at 5% to 20% weight fraction. Thus, in "acrylic" scintillator the active component is napthalene. The fluors must satisfy additional conditions besides being fluorescent. They must be sufficiently stable, soluble, chemically inert, fast, radiation tolerant, and efficient.

The plastic base is the ionization-sensitive (*i.e.*, the scintillator) portion of the plastic scintillator (see Fig. 27.1). In the absence of fluors the base would emit UV photons with short attenuation length (several mm). Longer attenuation lengths are obtained by dissolving a "primary" fluor in high concentration (1% by weight) into the base, which is selected to efficiently reradiate absorbed energy at wavelengths where the base is more transparent.

The primary fluor has a second important function. The decay time of the scintillator base material can be quite long—in pure polystyrene it is 16 ns, for example. The addition of the primary fluor in high concentration can shorten the decay time by an order of magnitude and increase the total light yield. At the concentrations used (1% and greater), the average distance between a fluor molecule and an excited base unit is around 100 Å, much less than a wavelength of light. At these distances the predominant mode of energy transfer from base to fluor is not the radiation of a photon, but a resonant dipole-dipole interaction, first described by Foerster, which strongly couples the base and fluor [9]. The strong coupling sharply increases the speed and the light yield of the plastic scintillators.

Unfortunately, a fluor which fulfills other requirements is usually not completely adequate with respect to emission wavelength or attenuation length, so it is necessary to add yet another waveshifter (the "secondary" fluor), at fractional percent levels, and occasionally a third (not shown in Fig. 27.1).

External wavelength shifters: Light emitted from a plastic scintillator may be absorbed in a (nonscintillating) base doped with a wave-shifting fluor. Such wavelength shifters are widely used to aid light collection in complex geometries. The wavelength shifter must be insensitive to ionizing radiation and Čerenkov light. A typical wavelength shifter uses an acrylic base (without napthalene!) because of its good optical qualities, a single fluor to shift the light emerging from the plastic scintillator to the blue-green, and contains ultra-violet absorbing additives to deaden response to Čerenkov light.

27.1.2. ***Caveats and cautions***: Plastic scintillators are reliable, robust, and convenient. However, they possess quirks to which the experimenter must be alert.

Aging and Handling: Plastic scintillators are subject to aging which diminishes the light yield. Exposure to solvent vapors, high temperatures, mechanical flexing, irradiation, or rough handling will aggravate the process. A particularly fragile region is the surface which can "craze"—develop microcracks—which rapidly destroy the capability of plastic scintillators to transmit light by total internal reflection. Crazing is particularly likely where oils, solvents, or *fingerprints* have contacted the surface.

Attenuation length: The Stokes' shift is not the only factor determining attenuation length. Others are the concentration of fluors (the higher the concentration of a fluor, the greater will be its self-absorption); the optical clarity and uniformity of the bulk material; the quality of the surface; and absorption by additives, such as stabilizers, which may be present.

Afterglow: Plastic scintillators have a long-lived luminescence which does not follow a simple exponential decay. Intensities at the 10^{-4} level of the initial fluorescence can persist for hundreds of ns [10].

Atmospheric quenching: Plastic scintillators will decrease their light yield with increasing partial pressure of oxygen. This can be a 10% effect in an artificial atmosphere [11]. It is not excluded that other gases may have similar quenching effects.

Magnetic field: The light yield of plastic scintillators may be changed by a magnetic field. The effect is very nonlinear and apparently not all types of plastic scintillators are so affected. Increases of $\approx 3\%$ at 0.45 T have been reported [12]. Data are sketchy and mechanisms are not understood.

Radiation damage: Irradiation of plastic scintillators creates color centers which absorb light more strongly in the UV and blue than at longer wavelengths. This poorly understood effect appears as a reduction both of light yield and attenuation length. Radiation damage depends not only on the integrated dose, but on the dose rate, atmosphere, and temperature, before, during and after irradiation, as well as the

materials properties of the base such as glass transition temperature, polymer chain length, *etc.* Annealing also occurs, accelerated by the diffusion of atmospheric oxygen and elevated temperatures. The phenomena are complex, unpredictable, and not well understood [13]. Since color centers are less intrusive at longer wavelengths, the most reliable method of mitigating radiation damage is to shift emissions at every step to the longest practical wavelengths, *e.g.*, utilize fluors with large Stokes' shifts.

27.1.3. *Scintillating and wavelength-shifting fibers*:

The clad optical fiber is an incarnation of scintillator and wavelength shifter (WLS) which is particularly useful [14]. Since the initial demonstration of the scintillating fiber (SCIFI) calorimeter [15], SCIFI techniques have become mainstream. SCIFI calorimeters are found, for example, in the g-2 experiment at Brookhaven [16] and at KLOE; SCIFI trackers are found at CHORUS and DØ ; WLS readout is used in both ATLAS and CMS hadron calorimeters [17].

SCIFI calorimeters are fast, dense, radiation hard, and can have leadglass-like resolution. SCIFI trackers can handle high rates and are radiation tolerant, but the low photon yield at the end of a long fiber (see below) forces the use of very sophisticated photodetectors such as VLPC's, such as are used in DØ . WLS scintillator readout of a calorimeter allows a very high level of hermeticity since the solid angle blocked by the fiber on its way to the photodetector is very small. The sensitive region of scintillating fibers can be controlled by splicing them onto clear (non-scintillating/non-WLS) fibers.

A typical configuration would be fibers with a core of polystyrene-based scintillator or WLS (index of refraction $n = 1.59$), surrounded by a cladding of PMMA ($n = 1.49$) a few microns thick, or, for added light capture, with another cladding of fluorinated PMMA with $n = 1.42$, for an overall diameter of 0.5 to 1 mm. The fiber is drawn from a boule and great care is taken during production to ensure that the intersurface between the core and the cladding has the highest possible uniformity and quality, so that the signal transmission via total internal reflection has a low loss. The fraction of generated light which is transported down the optical pipe is denoted the capture fraction and is about 6% for the single-clad fiber and 10% for the double-clad fiber.

The number of photons from the fiber available at the photodetector is always smaller than desired, and increasing the light yield has proven difficult [18]. A minimum-ionizing particle traversing a high-quality 1 mm diameter fiber perpendicular to its axis will produce fewer than 2000 photons, of which about 200 are captured. Attenuation eliminates about 95% of these photons. DØ uses 0.775 mm diameter scintillating fibers in the tracker and obtains 9 photoelectrons with the VLPC reaching 85% quantum efficiency.

A scintillating or WLS fiber is often characterized by its "attenuation length," over which the signal is attenuated to $1/e$ of its original value. Many factors determine the attenuation length, including the importance of re-absorption of emitted photons by the polymer base or dissolved fluors, the level of crystallinity of the base polymer, and the quality of the total internal reflection boundary. Attenuation lengths of several meters are obtained by high quality fibers. However, it should be understood that the attenuation length is not necessarily a measure of fiber quality. Among other things, it

is not constant with distance from the excitation source and it is wavelength dependent. So-called "cladding light" causes some of the distance dependence [19], but not all. The wavelength dependence is usually related to the higher re-absorption of shorter wavelength photons—once absorbed, re-emitted isotropically and lost with 90% probability—and to the lower absorption of longer wavelengths by polystyrene. Experimenters should be aware that measurements of attenuation length by a phototube with a bialkali photocathode, whose quantum efficiency drops below 10% at 480 nm, should not be naïvely compared to measurements utilizing a silicon photodiode, whose quantum efficiency is still rising at 600 nm.

27.2. Inorganic scintillators

Revised September 1999 by C.L. Woody (BNL).

Table 27.2 gives a partial list of commonly-used inorganic scintillators in high-energy and nuclear physics [20–27]. These scintillating crystals are generally used where high density and good energy resolution are required. In a crystal which contains nearly all of the energy deposited by an incident particle, the energy resolution is determined largely, but not totally, by the light output. The table gives the light output of the various materials relative to NaI, which has an intrinsic light output of about 40000 photons per MeV of energy deposit. The detected signal is usually quoted in terms of photoelectrons per MeV produced by a given photodetector. The relationship between photons/MeV produced and p.e.'s/MeV detected involves factors for light collection efficiency (typically 10–50%, depending on geometry) and the quantum efficiency of the detector ($\sim$ 15–20% for photomultiplier tubes and $\sim$ 70% for silicon photodiodes for visible wavelengths). The quantum efficiency of the detector is usually highly wavelength dependent and should be matched to the particular crystal of interest to give the highest quantum yield at the wavelength corresponding to the peak of the scintillation emission. The comparison of the light output given in Table 27.2 is for a standard photomultiplier tube with a bialkali photocathode. Results with photodiodes can be significantly different; *e.g.*, the CsI(Tl) response relative to NaI(Tl) is 1.4 rather than 0.40 [27]. For scintillators which emit in the UV, a detector with a quartz window should be used.

27.3. Čerenkov detectors

Written October 1993 by D.G. Coyne (UCSC).

Čerenkov detectors utilize one or more of the properties of Čerenkov radiation discussed in the Passages of Particles through Matter section (Sec. 26 of this *Review*): the existence of a *threshold* for radiation; the dependence of the Čerenkov cone half-angle θ_c on the *velocity* of the particle; the dependence of the *number of emitted photons* on the particle's velocity. The presence of the refractive index n in the relations allows tuning these quantities for a particular experimental application (*e.g.*, using pressurized gas and/or various liquids as radiators).

The number of photoelectrons (p.e.'s) detected in a given device or channel is

$$N_{\rm p.e.} = L\frac{\alpha^2 z^2}{r_e\, m_e c^2}\int \epsilon_{\rm coll}(E)\,\epsilon_{\rm det}(E)\sin^2\theta_c(E)dE\ , \qquad (27.2)$$

Table 27.2: Properties of several inorganic crystal scintillators. Notation for ρ, λ_I, n_D, *etc.*, is defined in the Table of Atomic and Nuclear Properties—Sec. 6 of this *Review*.

Crystal	ρ (g/cm^3)	X_0 (cm)	$r_{\text{Molière}}$ (cm)	dE/dx (MeV/cm)	λ_I (cm)	τ_{decay} (ns)	$\lambda_{\max}$	n_D	Rel. output*	Hygro?
NaI(Tl)	3.67	2.59	4.5	4.8	41.4	250	410	1.85	1.00	very
BGO	7.13	1.12	2.4	9.2	22.0	300	410	2.20	0.15	no
BaF_2	4.89	2.05	3.4	6.6	29.9	0.7^f	220^f	1.56	0.05^f	slightly
						620^s	310^s		0.20^s	
CsI(Tl)	4.53	1.85	3.8	5.6	36.5	1000	565	1.80	0.40	some
CsI(pure)	4.53	1.85	3.8	5.6	36.5	$10, 36^f$	305^f	1.80	0.10^f	some
						$36^f, 620^s$	$\sim 480^s$		0.20^s	
$PbWO_4$	8.28	0.89	2.2	13.0	22.4	5–15	420–440†	2.3	0.01	no
CeF_3	6.16	1.68	2.6	7.9	25.9	10–30	310–340	1.68	0.10	no

* For standard photomultiplier tube with a bialkali photocathode. See Ref. 27 for photo-diode results.

† Emission ~ 500 nm also possible due to crystal defects.

f = fast component, s = slow component

where L is the path length in the radiator, ϵ_{coll} is the efficiency for collecting the Čerenkov light, ϵ_{det} is the quantum efficiency of the transducer (photomultiplier or equivalent), and $\alpha^2/(r_e\, m_e c^2) = 370\ \text{cm}^{-1}\text{eV}^{-1}$. The quantities ϵ_{coll}, ϵ_{det}, and θ_c are all functions of the photon energy E, although in typical detectors θ_c (or, equivalently, the index of refraction) is nearly constant over the useful range of photocathode sensitivity. In this case,

$$N_{\text{p.e.}} \approx L N_0 \langle \sin^2 \theta_c \rangle \tag{27.3}$$

with

$$N_0 = \frac{\alpha^2 z^2}{r_e\, m_e c^2} \int \epsilon_{\text{coll}}\, \epsilon_{\text{det}}\, dE\ . \tag{27.4}$$

We take $z = 1$, the usual case in high-energy physics, in the following discussion.

Threshold Čerenkov detectors make a simple yes/no decision based on whether the particle is above/below the Čerenkov threshold velocity $\beta_t = 1/n$. Careful designs give $\langle \epsilon_{\text{coll}} \rangle \gtrsim 90\%$. For a photomultiplier with a typical bialkali cathode, $\int \epsilon_{\text{det}} dE \approx 0.27$, so that

$$N_{\text{p.e.}}/L \approx 90\ \text{cm}^{-1}\, \langle \sin^2 \theta_c \rangle \quad (\textit{i.e.}, N_0 = 90\ \text{cm}^{-1})\ . \tag{27.5}$$

Suppose, for example, that n is chosen so that the threshold for species a is p_t; that is, at this momentum species a has velocity $\beta_a = 1/n$. A second, lighter, species b with the

same momentum has velocity β_b, so $\cos\theta_c = \beta_a/\beta_b$, and

$$\frac{N_{\rm p.e.}}{L} \approx 90 \text{ cm}^{-1} \frac{m_a^2 - m_b^2}{p_t^2 + m_a^2} \ . \tag{27.6}$$

For K/π separation at $p = 1$ GeV/c, $N_{\rm p.e.}/L \approx 16$ cm^{-1} for π's and (by design) 0 for K's.

For limited path lengths $N_{\rm p.e.}$ can be small, and some minimum number is required to trigger external electronics. The overall efficiency of the device is controlled by Poisson fluctuations, which can be especially critical for separation of species where one particle type is dominant [28].

A related class of detectors uses the number of observed photoelectrons (or the calibrated pulse height) to discriminate between species or to set probabilities for each particle species [29].

Differential Čerenkov detectors exploit the dependence of θ_c on β, using optical focusing and/or geometrical masking to select particles having velocities in a specified region. With careful design, a velocity resolution of $\sigma_\beta/\beta \approx 10^{-4}$–$10^{-5}$ can be obtained [28,30].

Ring-Imaging Čerenkov detectors use all three properties of Čerenkov radiation in both small-aperture and 4π geometries. They are principally used as hypothesis-testing rather than yes/no devices; that is, the probability of various identification possibilities is established from θ_c and $N_{\rm p.e.}$ for a particle of known momentum. In most cases the optics map the Čerenkov cone onto a circle at the photodetector, often with distortions which must be understood.

The 4π devices [31,32] typically have both liquid (C_6F_{14}, $n = 1.276$) and gas (C_5F_{12}, $n = 1.0017$) radiators, the light from the latter being focused by mirrors. They achieve 3 σ separation of $e/\pi/K/p$ over wide ranges, as shown in Table 27.3. Great attention to detail, especially with the minimization of UV-absorbing impurities, is required to get $\langle\epsilon_{\rm coll}\rangle \gtrsim 50\%$.

Table 27.3: Momentum range for 3σ separation in the SLD ring-imaging Čerenkov detector.

Particle pair	Mom. range for 3 σ separation
e/π	$p \lesssim 5$ GeV/c
π/K	$0.23 \lesssim p \lesssim 20$ GeV/c
K/p	$0.82 \lesssim p \lesssim 30$ GeV/c

The phototransducer is typically a TPC/wire-chamber combination sensitive to single photoelectrons and having charge division or pads. This construction permits three-dimensional reconstruction of photoelectron origins, which is important for transforming the Čerenkov cone into a ring. Single photoelectrons are generated by doping the

TPC gas (for instance, ethane/methane in some proportion) with $\sim 0.05\%$ TMAE [tetrakis(dimethylamino)ethylene] [33], leading to photon absorption lengths along the Čerenkov cone of ~ 30 mm. The readout wires must be equipped with special structures (blinds or wire gates) to prevent photon feedback from avalanches generating cross-talk photoelectrons in the TPC. Drift-gas purity must be maintained to assure mean drift lengths of the order of meters without recombination (*i.e.*, lifetimes of $\gtrsim 100$ μs at typical drift velocities of $\gtrsim 4$ cm/μs). The net $\langle\epsilon_{\rm det}\rangle$'s reach 30%, with the limitation being the TMAE quantum efficiency.

Photon energy cutoffs are set by the TMAE ($E > 5.4$ eV), the UV transparency of fused silica glass ($E < 7.4$ eV), and the C_6F_{14} ($E < 7.1$ eV). With effort one gets $50 \leq N_0 \leq 100$ for complete rings using liquid or gas. This includes losses due to electrostatic shielding wires and window/mirror reflections, but not gross losses caused by total internal reflection or inadequate coverage by the TPC's.

Such numbers allow determination of ring radii to $\sim$0.5% (liquid) and $\sim$2% (gas), leading to the particle species separations quoted above. Since the separation efficiencies may have "holes" as a function of p, detailed calculations are necessary.

27.4. Transition radiation detectors (TRD's)

Revised February 1998 by D. Froidevaux (CERN).

It is clear from the discussion in the Passages of Particles Through Matter section (Sec. 26 of this *Review*) that transition radiation (TR) only becomes useful for particle detectors when the signal can be observed as x rays emitted along the particle direction for Lorentz factors γ larger than 1000. In practice, TRD's are therefore used to provide electron/pion separation for $0.5\ {\rm GeV}/c \lesssim p \lesssim 100\ {\rm GeV}/c$. The charged-particle momenta have usually been measured elsewhere in the detector in the past [34].

Since soft x rays, in the useful energy range between 2 and 20 keV, are radiated with about 1% probability per boundary crossing, practical detectors use radiators with several hundred interfaces, *e.g.* foils or fibers of low-Z materials such as polypropylene (or, more rarely, lithium) in a gas. Absorption inside the radiator itself and in the inactive material of the x-ray detector is important and limits the usefulness of the softer x rays, but interference effects are even larger, and saturate the x-ray yield for electron energies above a few GeV [35,36].

A classical detector is composed of several similar modules, each consisting of a radiator and an x-ray detector, which is usually a wire chamber operated with a xenon-rich mixture, in order efficiently to absorb the x rays. Since transition-radiation photons are mostly emitted at very small angles with respect to the charged-particle direction, the x-ray detector most often detects the sum of the ionization loss (dE/dx) of the charged particle in the gas and energy deposition of the x rays. The discrimination between electrons and pions can be based on the charges measured in each detection module, on the number of energy clusters observed above an optimal threshold (usually in the 5 to 7 keV region), or on more sophisticated methods analyzing the pulse shape as a function of time. Once properly calibrated and optimized, most of these methods yield very similar results.

More recent development work has aimed at increasing the intrinsic quality of the TRD-performance by increasing the probability per detection module of observing a signal from TR-photons produced by electrons. This has been achieved experimentally by distributing small-diameter straw-tube detectors uniformly throughout the radiator material [37]. This method has thereby also cured one of the major drawbacks of more classical TRD's, that is, their need to rely on another detector to measure the charged-particle trajectory. For example, in the straw tracker proposed for one of the LHC experiments [38], charged particles cross about 40 straw tubes embedded in the radiator material. Dedicated R&D work and detailed simulations have shown that the combination of charged-track measurement and particle identification in the same detector will provide a very powerful tool even at the highest LHC luminosity.

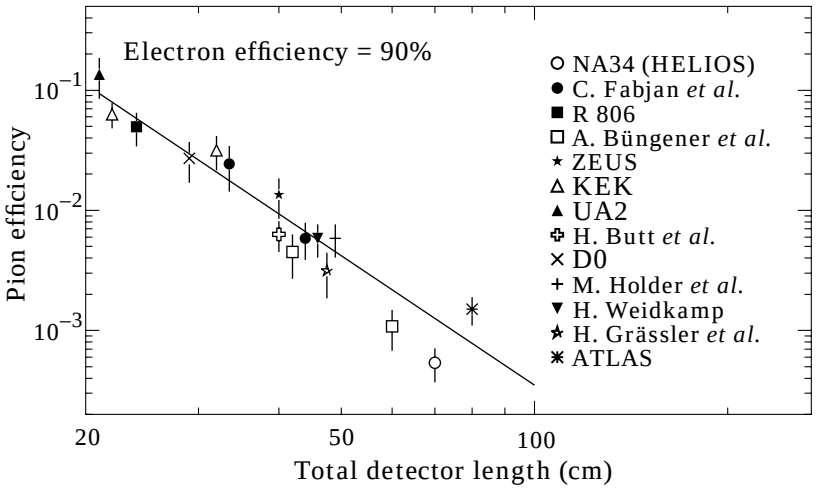

Figure 27.2: Pion efficiency measured (or predicted) for different TRDs as a function of the detector length for a fixed electron efficiency of 90%. The experimental data are directly taken or extrapolated from references [39–51] (top to bottom).

The major factor in the performance of any TRD is its overall length. This is illustrated in Fig. 27.2, which shows, for a variety of detectors, the measured (or predicted) pion efficiency at a fixed electron efficiency of 90% as a function of the overall detector length. The experimental data cover too wide a range of particle energies (from a few GeV to 40 GeV) to allow for a quantitative fit to a universal curve. Fig. 27.2 shows that an order of magnitude in rejection power against pions is gained each time the detector length is increased by ~ 20 cm.

27.5. Wire chambers

Written October 1999 by A. Cattai and L. Rolandi (CERN).

A wire chamber relies on the detection of a large fraction of the charge created in a volume filled with an appropriate gas mixture. A charged particle traversing a gas layer of thickness Δ produces electron-ion pairs along its path (see Sec. 26.2). The yield $(1/\lambda)$ of ionization encounters for a minimum ionization particle (m.i.p.) (see Fig. 26.1) is given in Table 27.4

Table 27.4: For various gases at STP: (a) yield of ionization encounters $(1/\lambda)$ for m.i.p. [52], (b) t_{99}: thickness of the gas layer for 99% efficiency, and (c) the average number of free electrons produced by a m.i.p. (calculated using data from Ref. 53).

	Encounters/cm	t_{99}(mm)	Free electrons/cm
He	5	9.2	16
Ne	12	3.8	42
Ar	25	1.8	103
Xe	46	1.0	340
CH_4	27	1.7	62
CO_2	35	1.3	107
C_2H_6	43	1.1	113

The probability to have at least one ionization encounter is $1 - \exp(-\Delta/\lambda)$ and the thickness of the gas layer for 99% efficiency is $t_{99} = 4.6\lambda$. Depending on the gas, some 65–80% of the encounters result in the production of only one electron; the probability that a cluster has more than five electrons is smaller than 10%. However the tail of the distribution is very long and the yield of ionization electrons is 3–4 times that of the ionization encounters. The secondary ionization happens either in collisions of (primary) ionization electrons with atoms or through intermediate excited states. The process is non-linear and gas mixtures may have larger yields than each of their components. See also the discussion in Sec. 26.7.

Under the influence of electric and magnetic fields the ionization electrons drift inside the gas with velocity $\boldsymbol{u}$ given by:

$$\boldsymbol{u} = \mu|\boldsymbol{E}|\frac{1}{1+\omega^2\tau^2}\left(\widehat{\boldsymbol{E}} + \omega\tau(\widehat{\boldsymbol{E}}\times\widehat{\boldsymbol{B}}) + \omega^2\tau^2(\widehat{\boldsymbol{E}}\cdot\widehat{\boldsymbol{B}})\widehat{\boldsymbol{B}}\right) \tag{27.7}$$

where $\widehat{\boldsymbol{E}}$ and $\widehat{\boldsymbol{B}}$ are unit vectors in the directions of the electric and magnetic fields respectively, μ is the electron mobility in the gas, ω is the cyclotron frequency eB/mc, and $\tau = \mu m/e$ is the mean time between collisions of the drifting electrons. The magnitude of the drift velocity depends on many parameters; typical values are in the range 1–8 cm/μs.

In a quite common geometry, the drift electric field is perpendicular to the magnetic field. In this case the electrons drift at an angle ψ with respect to the electric field direction such that $\tan\psi = \omega\tau$.

The ionization electrons are eventually collected by a thin (typically 10 μm radius) anode wire where a strong electric field—increasing as $1/r$—accelerates the electrons enough to produce secondary ionization and hence an avalanche. A quenching gas (organic molecules with large photo-absorption cross-section) absorbs the majority of the photons produced during the avalanche development, keeping the avalanche region localized. The gain achievable with a wire counter depends exponentially on the charge density on the wire, on the gas density ρ and—through it—on pressure and temperature: $dG/G \approx -Kd\rho/\rho$, where the coefficient K ranges between 5 and 8 in practical cases. Gains larger than 10^4 can be obtained in proportional mode.

The electrons produced in the avalanche are collected by the wire in a few nanoseconds. The positive ions move away from the wire and generate a signal that can be detected with an amplifier. Depending on whether the wire is treated as a current source or a voltage source, the signal is described respectively by:

$$I(t) = q\frac{d}{dt}F(t) \; ; \qquad \Delta V(t) = \frac{q}{C}F(t) \; , \tag{27.8}$$

where q is the positive charge in the avalanche, C is the capacitance between the anode wire and the cathodes and $F(t) = \ln(1 + t/t_0)/\ln(1 + t_{\max}/t_0)$. The constant t_0 is of the order of one or few nanoseconds; the constant $t_{\max}$ (several microseconds) describes the time that it takes ions to reach the cathodes.

A sketch of the first multi-wire proportional chamber (MWPC) [54] is shown in Fig. 27.3. It consists of a plane of parallel sense wires with spacing s and length L inserted in a gap of thickness Δ. The potential distributions and fields in a proportional or drift chamber can usually be calculated with good accuracy from the exact formula for the potential around an array of parallel line charges q (coul/m) along z and located at $y = 0$, $x = 0$, $\pm s$, $\pm 2s$, ...,

$$V(x, y) = -\frac{q}{4\pi\,\epsilon_0} \ln\left\{4\left[\sin^2\left(\frac{\pi x}{s}\right) + \sinh^2\left(\frac{\pi y}{s}\right)\right]\right\} \; . \tag{27.9}$$

With digital readout, the resolution in the direction perpendicular to the wire is $s/\sqrt{12}$, where s is typically 1–2 mm. Similar resolution can be achieved with a smaller channel density by measuring the difference in time between the arrival of electrons at the wire and the traversal of the particle, albeit with a longer response time. In the case of drift chambers, the spatial resolution is limited by the diffusion of ionization electrons during the drift and by the fluctuations of the ionization process. Depending on the gas mixture, the width of the diffusing cloud after 1 cm of drift is typically between 50 and 300 μm; small diffusion implies low drift velocity. With drift lengths up to 5 cm (1 μs), resolutions in the range 100–200 μm have been achieved in chambers with surface areas of several square meters [56]. The central detectors in many collider experiments are drift chambers with the wires parallel to the beam direction. Small volume chambers (0.1 m^3) have been used for vertex measurement achieving resolutions of 50 μm using high pressure (2–4 bar) and low diffusion gas mixtures [57]. Large volume chambers (5–40 m^3) with several thousand wires of length of 1–2 meters are operated with resolution between 100 and 200 μm [58].

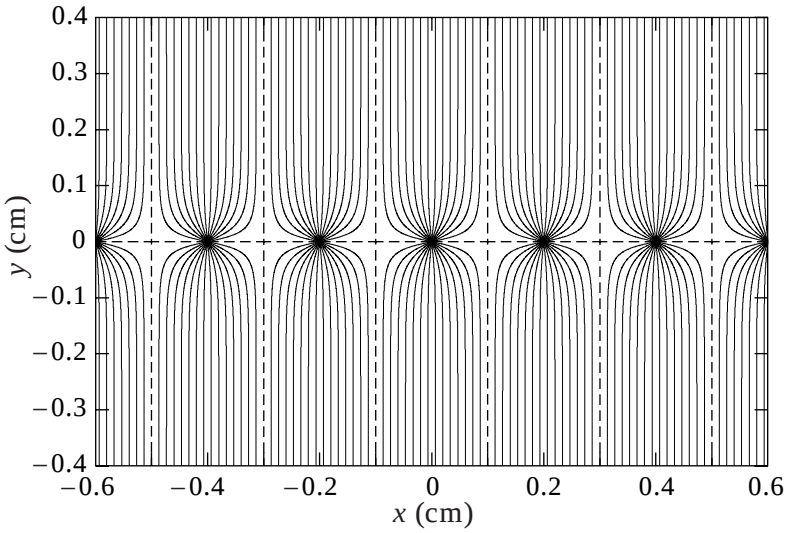

Figure 27.3: Electric field lines in a (MWPC) with an anode pitch of 2 mm as calculated with GARFIELD program [55].

The spatial resolution cannot be improved by arbitrarily reducing the spacing of the wires. In addition to the practical difficulties of precisely stringing wires at a pitch below 1 mm, there is a fundamental limitation: the electrostatic force between the wires is balanced by the mechanical tension, which cannot exceed a critical value. This gives the following approximate stability condition:

$$\frac{s}{L} \geq 1.5 \times 10^{-3} V(\mathrm{kV}) \sqrt{\frac{20\ \mathrm{g}}{T}}\ , \tag{27.10}$$

where V is the voltage of the sense wire and T is the tension of the wire in grams-weight equivalent.

This limitation can be overcome by means of lithographic techniques [59]: a series of thin aluminum strips are precisely 0.2 μm engraved on an insulating support producing a miniaturized version of a MWPC (see Fig. 27.4). With this technique the spacing of the anodes can be reduced to 0.1–0.2 mm, reducing the drift time of the ions and improving on the spatial resolution and on the rate capability of the chamber.

In all these devices, since the avalanche is very localized along the anode, signals induced on nearby electrodes can be used to measure the coordinate along the anode direction (see Sec. 27.6).

A review of the principle of particle detection with drift chambers can be found in [60]. A compilation of the mobilities, diffusion coefficients and drift deflection angles as a function of $\boldsymbol{E}$ and $\boldsymbol{B}$ for several gas mixtures used in proportional chambers can be found in [61]. A review of micro-strip gas chambers (MSGC) can be found in [62].

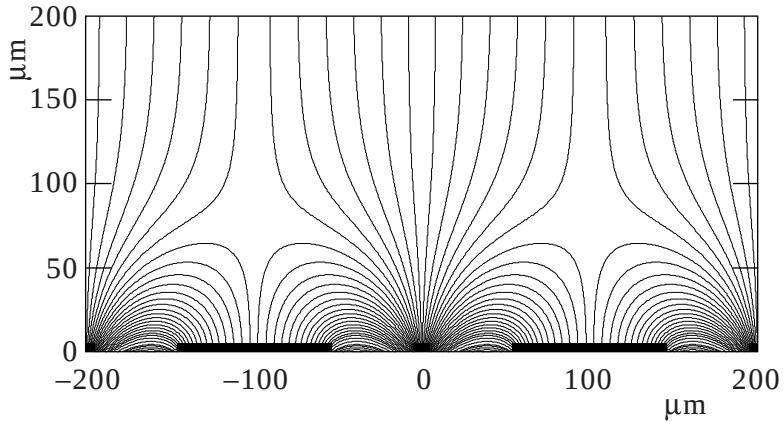

Figure 27.4: Electron drift lines in a micro-strip gas chamber with a pitch of 200 μm.

27.6. Time-projection chambers

Written November 1997 by M.T. Ronan (LBNL).

Detectors with long drift distances perpendicular to a multi-anode proportional plane provide three-dimensional information, with one being the time projection. A (typically strong) magnetic field parallel to the drift direction suppresses transverse diffusion ($\sigma = \sqrt{2Dt}$) by a factor

$$D(B)/D(0) = \frac{1}{1+\omega^2\tau^2} \ , \tag{27.11}$$

where D is the diffusion coefficient, $\omega = eB/mc$ is the cyclotron frequency, and τ is the mean time between collisions. Multiple measurements of dE/dx along the particle trajectory combined with the measurement of momentum in the magnetic field allows excellent particle identification [63], as can be seen in Fig. 27.5.

A typical gas-filled TPC consists of a long uniform drift region (1–2 m) generated by a central high-voltage membrane and precision concentric cylindrical field cages within a uniform, parallel magnetic field [60]. Details of construction and electron trajectories near the anode end are shown in Fig. 27.6. Signal shaping and processing using analog storage devices or FADC's allows excellent pattern recognition, track reconstruction, and particle identification within the same detector.

Typical values:

Gas: Ar + (10–20%) CH_4	Pressure(P) = 1–8.5 atm.
E/P = 100–200 V/cm/atm	B = 1–1.5 Tesla
$v_{\rm drift}$ = 5–7 cm/μs	$\omega\tau$ = 1–8
$\sigma_{x \text{ or } y}$ = 100–200 μm	σ_z = 0.2–1 mm
$\sigma_{dE/dx}$ = 2.5–5.5 %	

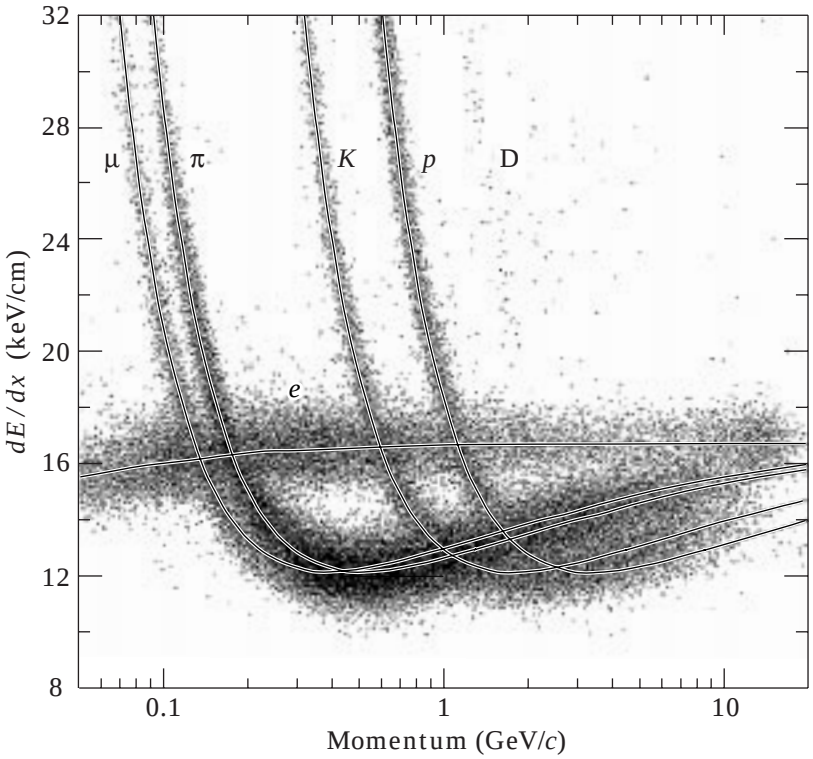

Figure 27.5: PEP4/9-TPC dE/dx measurements (185 samples @8.5 atm Ar-CH_4 80–20%) in multihadron events. The electrons reach a Fermi plateau value of 1.4 times minimum. Muons from pion decays are separated from pions at low momentum; π/K are separated over all momenta except in the cross-over region. (Low-momentum protons and deuterons originate from hadron-nucleus collisions in inner materials such as the beam pipe.)

Truncated mean dE/dx resolution depends on the number and size of samples, and gas pressure:

$$\sigma_{dE/dx} \propto N^{-0.43} \times (P\ell)^{-0.32} \ . \tag{27.12}$$

Here N is the number of samples, ℓ is the sample size, and P is the pressure. Typical dE/dx distributions are shown in Fig. 27.5. Good three-dimensional two-track resolutions of about 1–1.5 cm are routinely achieved.

$E \times B$ distortions arise from nonparallel E and B fields (see Eq. (27.7)), and from the curved drift of electrons to the anode wires in the amplification region. Position measurement errors include contributions from the anode-cathode geometry, the track crossing angle (α), $E \times B$ distortions, and from the drift diffusion of electrons

$$\sigma^2_{x \text{ or } y} = \sigma_0^2 + \sigma_D^2(1 + \tan^2\alpha)L/L_{\max} + \sigma_\alpha^2(\tan\alpha - \tan\psi)^2 \tag{27.13}$$

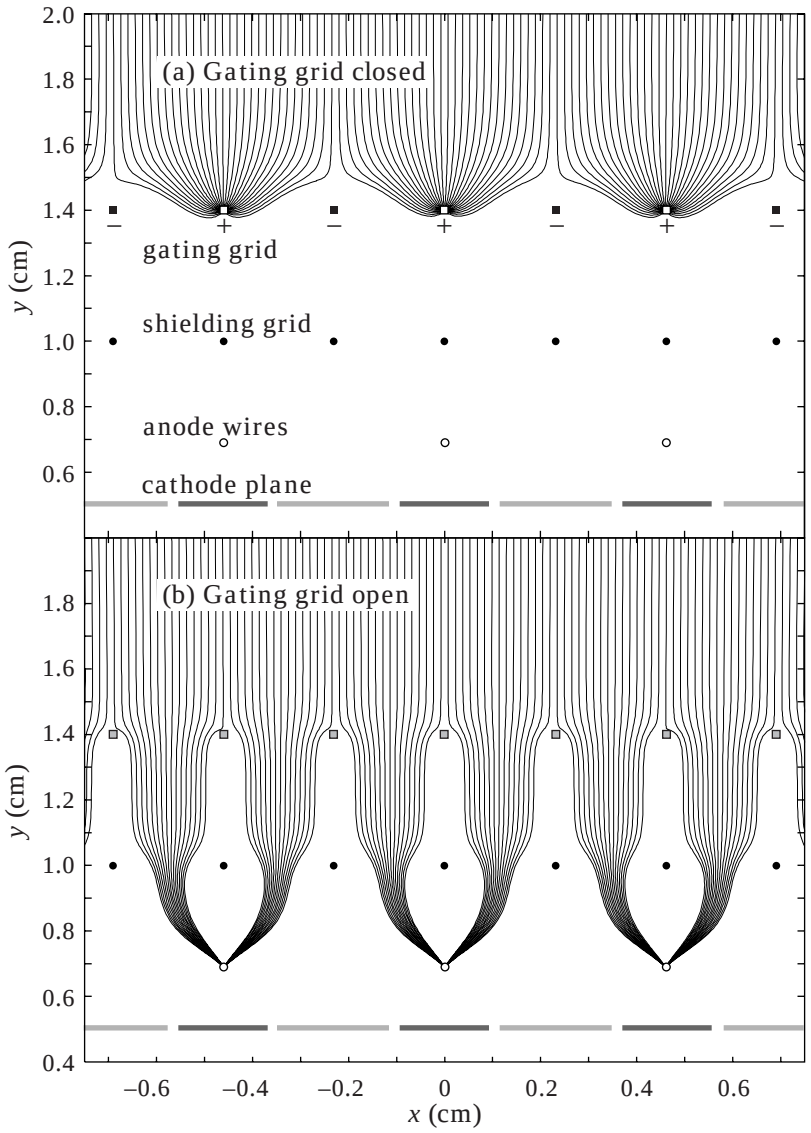

Figure 27.6: (a) Drifting electrons are collected on the gating grid until gated open by a triggering event. A shielding grid at ground potential is used to terminate the drift region. Electrons drifting through an open gating grid (b) pass through to the amplification region around the anode wires. Positive ions generated in the avalanche are detected on segmented cathode pads to provide precise measurements along the wire. The slow positive ions are blocked from entering the drift region by closing the gating grid after the electrons have drifted through.

where σ is the coordinate resolution, σ_0 includes the anode-cathode geometry contribution, ψ is the Lorentz angle, and L is the drift distance.

Space-charge distortions arise in high-rate environments, especially for low values of $\omega\tau$. However, they are mitigated by an effective gating grid (Fig. 27.6). Field uniformities of

$$\int (E_\perp/E)\, dz \lesssim 0.5\text{–}1 \text{ mm} , \tag{27.14}$$

over 10–40 m^3 volumes have been obtained. Laser tracks and calibration events allow mapping of any remnant drift non-uniformities.

27.7. Silicon semiconductor detectors

Updated September 2001 by H.G. Spieler (LBNL).

Semiconductor detectors are widely used in modern high-energy physics experiments. They are the key ingredient of high-resolution vertex and tracking detectors and are also used as photodetectors in scintillation calorimeters. The most commonly used material is silicon, but germanium, gallium-arsenide and diamond are also useful in some applications. Integrated circuit technology allows the formation of high-density micron-scale electrodes on large (10–15 cm diameter) wafers, providing excellent position resolution. Furthermore, the density of silicon and its small ionization energy result in adequate signals with active layers only 100–300 μm thick, so the signals are also fast (typically tens of ns). Semiconductor detectors depend crucially on low-noise electronics (see Sec. 27.8), so the detection sensitivity is determined by signal charge and capacitance. For a survey of recent developments see Ref. 64.

Silicon detectors are *p*-*n* junction diodes operated at reverse bias. This forms a sensitive region depleted of mobile charge and sets up an electric field that sweeps charge liberated by radiation to the electrodes. Detectors typically use an asymmetric structure, e.g. a highly doped p electrode and a lightly doped n region, so that the depletion region extends predominantly into the lightly doped volume. The thickness of the depleted region is

$$W = \sqrt{2\epsilon\,(V + V_{bi})/Ne} = \sqrt{2\rho\mu\epsilon(V + V_{bi})} , \tag{27.15}$$

where $V =$ external bias voltage

$V_{bi} =$ "built-in" voltage (≈ 0.5 V for resistivities typically used in detectors)

$N =$ doping concentration

$e =$ electronic charge

$\epsilon =$ dielectric constant $= 11.9\ \epsilon_0 \approx 1$ pF/cm

$\rho =$ resistivity (typically 1–10 kΩ cm)

$\mu =$ charge carrier mobility

$= 1350$ cm^2 V^{-1} s^{-1} for electrons (n-type material)

$= 450$ cm^2 V^{-1} s^{-1} for holes (p-type material)

or

$$W = 0.5\ [\mu\text{m}/\sqrt{\Omega\text{-cm}\cdot\text{V}}] \times \sqrt{\rho(V + V_{bi})}\ \text{ for } n\text{-type material, and} \tag{27.16}$$

$$W = 0.3\ [\mu\text{m}/\sqrt{\Omega\text{-cm}\cdot\text{V}}] \times \sqrt{\rho(V + V_{bi})}\ \text{ for } p\text{-type material.} \tag{27.17}$$

The conductive p and n regions together with the depleted volume form a capacitor with the capacitance per unit area

$$C = \epsilon/W \approx 1\,[\text{pF/cm}]\,/W\ . \tag{27.18}$$

In strip and pixel detectors the capacitance is dominated by the fringing capacitance. For example, the strip-to-strip fringing capacitance is $\sim$ 1–1.5 pF cm^{-1} of strip length at a strip pitch of 25–50 μm.

For energetic particles and photons the energy required to create an electron-hole pair E_i = 3.6 eV (which is larger than the band gap because phonon excitation is required for momentum conservation). For minimum-ionizing particles, the most probable charge deposition in a 300 μm thick silicon detector is about 3.5 fC (22000 electrons). Since both electronic and lattice excitations are involved, the variance in the number of charge carriers $N = E/E_i$ produced by an absorbed energy E is reduced by the Fano factor F (about 0.1 in Si). Thus, $\sigma_N = \sqrt{FN}$ and the energy resolution $\sigma_E/E = \sqrt{FE_i/E}$. However, the measured signal fluctuations are usually dominated by electronic noise or energy loss fluctuations in the detector. Visible light can be detected with photon energies above the band gap. In optimized photodiodes quantum efficiencies $> 80\%$ for wavelengths between 400 nm and nearly 1 μm are achievable. UV-extended photodiodes have useful efficiency down to 200 nm.

Charge collection time decreases with increasing bias voltage, and can be reduced further by operating the detector with "overbias," *i.e.*, a bias voltage exceeding the value required to fully deplete the device. The collection time is limited by velocity saturation at high fields (approaching 10^7 cm/s at $E > 10^4$ V/cm); at an average field of 10^4 V/cm the collection time is about 15 ps/μm for electrons and 30 ps/μm for holes. In typical fully-depleted detectors 300 μm thick, electrons are collected within about 10 ns, and holes within about 25 ns.

Position resolution is limited by transverse diffusion during charge collection (typically 5 μm for 300 μm thickness) and by knock-on electrons. Resolutions of 2–4 μm (rms) have been obtained in beam tests. In magnetic fields, the Lorentz drift deflects the electron and hole trajectories and the detector must be tilted to reduce spatial spreading (see "Hall effect" in semiconductor textbooks).

Radiation damage occurs through two basic mechanisms:

1. Bulk damage due to displacement of atoms from their lattice sites. This leads to increased leakage current, carrier trapping, and build-up of space charge that changes the required operating voltage. Displacement damage depends on the nonionizing energy loss and the energy imparted to the recoil atoms, which can initiate a chain of subsequent displacements, *i.e.*, damage clusters. Hence, it is critical to consider both particle type and energy.

2. Surface damage due to charge build-up in surface layers, which leads to increased surface leakage currents. In strip detectors the inter-strip isolation is affected. The effects of charge build-up are strongly dependent on the device structure and on fabrication details. Since the damage is proportional to the absorbed energy (when ionization dominates), the dose can be specified in rad (or Gray) independent of particle type.

The increase in reverse bias current due to bulk damage is $\Delta I_r = \alpha\Phi$ per unit volume, where Φ is the particle fluence and α the damage coefficient ($\alpha \approx 3 \times 10^{-17}$ A/cm for minimum ionizing protons and pions after long-term annealing; $\alpha \approx 2 \times 10^{-17}$ A/cm for 1 MeV neutrons). The reverse bias current depends strongly on temperature

$$\frac{I_R(T_2)}{I_R(T_1)} = \left(\frac{T_2}{T_1}\right)^2 \exp\left[-\frac{E}{2k}\left(\frac{T_1 - T_2}{T_1 T_2}\right)\right] \tag{27.19}$$

where $E = 1.2$ eV in irradiated Si, so rather modest cooling can reduce the current substantially ($\sim$ 6-fold current reduction in cooling from room temperature to 0°C).

The space-charge concentration in high-resistivity n-type Si changes approximately as

$$N = N_0 e^{-\delta\Phi} - \beta\Phi \ , \tag{27.20}$$

where N_0 is the initial donor concentration, $\delta \approx 6 \times 10^{-14}$ cm^2 determines donor removal, and $\beta \approx 0.03$ cm^{-1} describes acceptor creation. The acceptor states trap electrons, building up a negative space charge, which in turn requires an increase in the applied voltage to sweep signal charge through the detector thickness. This has the same effect as a change in resistivity, *i.e.*, the required voltage drops initially with fluence, until the positive and negative space charge balance and very little voltage is required to collect all signal charge. At larger fluences the negative space charge dominates, and the required operating voltage increases ($V \propto N$). The safe operating limit of depletion voltage ultimately limits the detector lifetime. Since the effect of radiation damage depends on the electronic activity of defects, various techniques have been applied to neutralize the damage sites. For example, additional doping with oxygen increases the allowable charged hadron fluence substantially (factors of two to three have been demonstrated) [65]. The increase in leakage current, on the other hand, is independent of doping or processing.

Strip and pixel detectors have remained functional at fluences beyond 10^{15} cm^{-2} for minimum ionizing protons. At this damage level, charge loss due to recombination and trapping also becomes significant and the high signal-to-noise ratio obtainable with low-capacitance pixel structures extends detector lifetime. The occupancy of the defect charge states is strongly temperature dependent; competing processes can increase or decrease the required operating voltage. It is critical to choose the operating temperature judiciously (-10 to 0°C in typical collider detectors) and limit warm-up periods during maintenance. For a more detailed summary see Ref. 66 and references therein.

27.8. Low-noise electronics

Written October 1999 by H. Spieler (LBNL).

Many detectors rely critically on low-noise electronics, either to improve energy resolution or to allow a low detection threshold. A typical detector front-end is shown in Fig. 27.7.

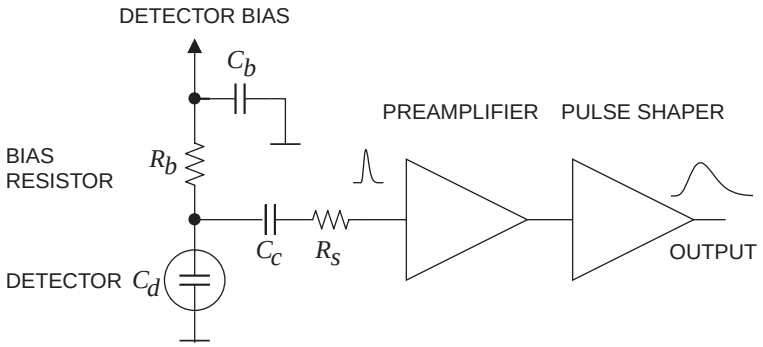

Figure 27.7: Typical detector front-end circuit.

The detector is represented by a capacitance C_d, a relevant model for most detectors. Bias voltage is applied through resistor R_b and the signal is coupled to the preamplifier through a blocking capacitor C_c. The series resistance R_s represents the sum of all resistances present in the input signal path, *e.g.* the electrode resistance, any input protection networks, and parasitic resistances in the input transistor. The preamplifier provides gain and feeds a pulse shaper, which tailors the overall frequency response to optimize signal-to-noise ratio while limiting the duration of the signal pulse to accommodate the signal pulse rate. Even if not explicitly stated, all amplifiers provide some form of pulse shaping due to their limited frequency response.

The equivalent circuit for the noise analysis (Fig. 27.8) includes both current and voltage noise sources. The leakage current of a semiconductor detector, for example, fluctuates due to electron emission statistics. This "shot noise" i_{nd} is represented by a current noise generator in parallel with the detector. Resistors exhibit noise due to thermal velocity fluctuations of the charge carriers. This noise source can be modeled either as a voltage or current generator. Generally, resistors shunting the input act as noise current sources and resistors in series with the input act as noise voltage sources (which is why some in the detector community refer to current and voltage noise as "parallel" and "series" noise). Since the bias resistor effectively shunts the input, as the capacitor C_b passes current fluctuations to ground, it acts as a current generator i_{nb} and its noise current has the same effect as the shot noise current from the detector. Any other shunt resistances can be incorporated in the same way. Conversely, the series resistor R_s acts as a voltage generator. The electronic noise of the amplifier is described fully by a combination of voltage and current sources at its input, shown as e_{na} and i_{na}.

Shot noise and thermal noise have a "white" frequency distribution, *i.e.* the spectral power densities $dP_n/df \propto di_n^2/df \propto de_n^2/df$ are constant with the magnitudes

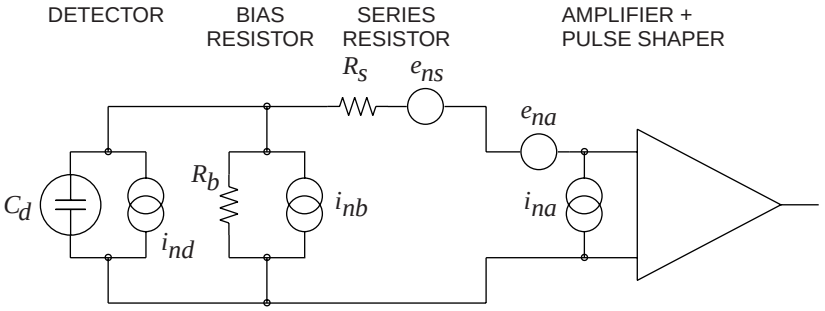

Figure 27.8: Equivalent circuit for noise analysis.

$$\begin{aligned} i_{nd}^2 &= 2eI_d \ , \\ i_{nb}^2 &= \frac{4kT}{R_b} \ , \\ e_{ns}^2 &= 4kTR_s \ , \end{aligned} \tag{27.21}$$

where e is the electronic charge, I_d the detector bias current, k the Boltzmann constant and T the temperature. Typical amplifier noise parameters e_{na} and i_{na} are of order $\mathrm{nV}/\sqrt{\mathrm{Hz}}$ and $\mathrm{pA}/\sqrt{\mathrm{Hz}}$. Trapping and detrapping processes in resistors, dielectrics and semiconductors can introduce additional fluctuations whose noise power frequently exhibits a $1/f$ spectrum. The spectral density of the $1/f$ noise voltage is

$$e_{nf}^2 = \frac{A_f}{f} \ , \tag{27.22}$$

where the noise coefficient A_f is device specific and of order 10^{-10}–$10^{-12}\,\mathrm{V}^2$.

A fraction of the noise current flows through the detector capacitance, resulting in a frequency-dependent noise voltage $i_n^2/(\omega C_d)^2$, which is added to the noise voltage in the input circuit. Since the individual noise contributions are random and uncorrelated, they add in quadrature. The total noise at the output of the pulse shaper is obtained by integrating over the full bandwidth of the system. Superimposed on repetitive detector signal pulses of constant magnitude, purely random noise produces a Gaussian signal distribution.

Since radiation detectors typically convert the deposited energy into charge, the system's noise level is conveniently expressed as an equivalent noise charge Q_n, which is equal to the detector signal that yields a signal-to-noise ratio of one. The equivalent noise charge is commonly expressed in Coulombs, the corresponding number of electrons, or the equivalent deposited energy (eV). For a capacitive sensor

$$Q_n^2 = i_n^2 F_i T_S + e_n^2 F_v \frac{C^2}{T_S} + F_{vf} A_f C^2 \ , \tag{27.23}$$

where C is the sum of all capacitances shunting the input, F_i, F_v, and F_{vf} depend on the shape of the pulse determined by the shaper and T_s is a characteristic time, for example, the peaking time of a semi-gaussian pulse or the sampling interval in a correlated double sampler. The form factors F_i, F_v are easily calculated

$$F_i = \frac{1}{2T_S}\int_{-\infty}^{\infty}[W(t)]^2\,dt\ , \qquad F_v = \frac{T_S}{2}\int_{-\infty}^{\infty}\left[\frac{dW(t)}{dt}\right]^2 dt\ , \tag{27.24}$$

where for time-invariant pulse-shaping $W(t)$ is simply the system's impulse response (the output signal seen on an oscilloscope) with the peak output signal normalized to unity. For more details see Refs. [67–68].

A pulse shaper formed by a single differentiator and integrator with equal time constants has $F_i = F_v = 0.9$ and $F_{fv} = 4$, independent of the shaping time constant. The overall noise bandwidth, however, depends on the time constant, *i.e.* the characteristic time T_s. The contribution from noise currents increases with shaping time, *i.e.*, pulse duration, whereas the voltage noise decreases with increasing shaping time. Noise with a $1/f$ spectrum depends only on the ratio of upper to lower cutoff frequencies (integrator to differentiator time constants), so for a given shaper topology the $1/f$ contribution to Q_n is independent of T_s. Furthermore, the contribution of noise voltage sources to Q_n increases with detector capacitance. Pulse shapers can be designed to reduce the effect of current noise, *e.g.*, mitigate radiation damage. Increasing pulse symmetry tends to decrease F_i and increase F_v (*e.g.*, to 0.45 and 1.0 for a shaper with one CR differentiator and four cascaded integrators).

$$\begin{aligned} Q_n^2 = &\left(2eI_d + 4kT/R_b + i_{na}^2\right)F_iT_S \\ &+ \left(4kTR_s + e_{na}^2\right)F_vC_d^2/T_S + F_{vf}A_fC_d^2\ . \end{aligned} \tag{27.25}$$

As the characteristic time T_S is changed, the total noise goes through a minimum, where the current and voltage contributions are equal. Fig. 27.9 shows a typical example. At short shaping times the voltage noise dominates, whereas at long shaping times the current noise takes over. The noise minimum is flattened by the presence of $1/f$ noise. Increasing the detector capacitance will increase the voltage noise and shift the noise minimum to longer shaping times.

For quick estimates, one can use the following equation, which assumes an FET amplifier (negligible i_{na}) and a simple CR–RC shaper with time constants τ (equal to the peaking time):

$$\begin{aligned} (Q_n/e)^2 = &\,12\left[\frac{1}{\mathrm{nA\cdot ns}}\right]I_d\tau + 6\times10^5\left[\frac{\mathrm{k\Omega}}{\mathrm{ns}}\right]\frac{\tau}{R_b} \\ &+ 3.6\times10^4\left[\frac{\mathrm{ns}}{(\mathrm{pF})^2(\mathrm{nV})^2/\mathrm{Hz}}\right]e_n^2\frac{C^2}{\tau}\ . \end{aligned} \tag{27.26}$$

Noise is improved by reducing the detector capacitance and leakage current, judiciously selecting all resistances in the input circuit, and choosing the optimum shaping time constant.

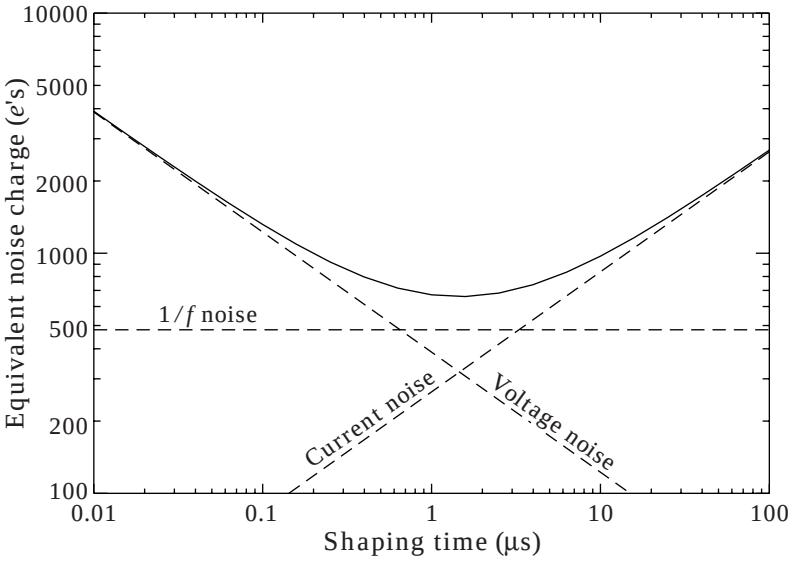

Figure 27.9: Equivalent noise charge vs shaping time.

The noise parameters of the amplifier depend primarily on the input device. In field effect transistors, the noise current contribution is very small, so reducing the detector leakage current and increasing the bias resistance will allow long shaping times with correspondingly lower noise. In bipolar transistors, the base current sets a lower bound on the noise current, so these devices are best at short shaping times. In special cases where the noise of a transistor scales with geometry, *i.e.*, decreasing noise voltage with increasing input capacitance, the lowest noise is obtained when the input capacitance of the transistor is equal to the detector capacitance, albeit at the expense of power dissipation. Capacitive matching is useful with field-effect transistors, but not bipolar transistors. In bipolar transistors, the minimum obtainable noise is independent of shaping time, but only at the optimum collector current I_C, which does depend on shaping time.

$$Q^2_{n,\min} = 4kT\frac{C}{\sqrt{\beta_{DC}}}\sqrt{F_i F_v} \;\text{ at }\; I_c = \frac{kT}{e}C\sqrt{\beta_{DC}}\sqrt{\frac{F_v}{F_i}}\frac{1}{T_S}\ , \tag{27.27}$$

where β_{DC} is the DC current gain. For a CR–RC shaper,

$$Q_{n,\min}/e \approx 800\Big[\frac{1}{\sqrt{\text{pF}}}\Big] \times \frac{\sqrt{C}}{(\beta_{DC})^{1/4}}\ . \tag{27.28}$$

Practical noise levels range from $\sim 1e$ for CCDs at long shaping times to $\sim 10^4$ e in high-capacitance liquid argon calorimeters. Silicon strip detectors typically operate at $\sim 10^3$ e electrons, whereas pixel detectors with fast readout provide noise of several hundred electrons.

In timing measurements, the slope-to-noise ratio must be optimized, rather than the signal-to-noise ratio alone, so the rise time t_r of the pulse is important. The "jitter" σ_t of the timing distribution is

$$\sigma_t = \frac{\sigma_n}{(dS/dt)_{S_T}} \approx \frac{t_r}{S/N} \ , \tag{27.29}$$

where σ_n is the rms noise and the derivative of the signal dS/dt is evaluated at the trigger level S_T. To increase dS/dt without incurring excessive noise, the amplifier bandwidth should match the rise-time of the detector signal. Increasing signal-to-noise ratio also improves time resolution, so minimizing the total capacitance at the input is also important. At high signal-to-noise ratios, the time jitter can be much smaller than the rise time. The timing distribution may shift with signal level ("walk"), but this can be corrected by various means, either in hardware or software [69].

27.9. Calorimeters

27.9.1. ***Electromagnetic calorimeters***:: The development of electromagnetic showers is discussed in the "Passage of Particles Through Matter" section (Sec. 26 of this *Review*). Formulae are given for the approximate description of average showers, but since the physics of electromagnetic showers is well understood, detailed and reliable Monte Carlo simulation is possible. EGS4 has emerged as the standard [70].

The resolution of sampling calorimeters (hadronic and electromagnetic) is usually dominated by sampling fluctuations, leading to fractional resolution σ/E scaling inversely as the square root of the incident energy. Homogeneous calorimeters, such as solid NaI(Tl), will in general not have resolution varying as $1/\sqrt{E}$. At high energies deviations from $1/\sqrt{E}$ occur because of noise, pedestal fluctuations, nonuniformities, calibration errors, and incomplete shower containment. Such effects are usually included by adding a constant term to σ/E, either in quadrature or (incorrectly) directly. In the case of the hadronic cascades discussed below, noncompensation also contributes to the constant term.

In Table 27.5 we give resolution as measured in detectors using typical EM calorimeter technologies. In almost all cases the installed calorimeters yield worse resolution than test beam prototypes for a variety of practical reasons. Where possible actual detector performance is given. For a fixed number of radiation lengths, the FWHM in sandwich detectors would be expected to be proportional to $\sqrt{t}$ for t (= plate thickness) ≥ 0.2 radiation lengths [71].

Given sufficient transverse granularity early in the calorimeter, position resolution of the order of a millimeter can be obtained.

Table 27.5: Resolution of typical electromagnetic calorimeters. E is in GeV.

Detector	Resolution
NaI(Tl) (Crystal Ball [72]; 20 X_0)	$2.7\%/E^{1/4}$
Lead glass (OPAL [73])	$5\%/\sqrt{E}$
Lead-liquid argon (NA31 [74]; 80 cells: 27 X_0, 1.5 mm Pb + 0.6 mm Al + 0.8 mm G10 + 4 mm LA)	$7.5\%/\sqrt{E}$
Lead-scintillator sandwich (ARGUS [75], LAPP-LAL [76])	$9\%/\sqrt{E}$
Lead-scintillator spaghetti (CERN test module) [77]	$13\%/\sqrt{E}$
Proportional wire chamber (MAC; 32 cells: 13 X_0, 2.5 mm typemetal + 1.6 mm Al) [78]	$23\%/\sqrt{E}$

27.9.2. ***Hadronic calorimeters***: [80,81] The length scale appropriate for hadronic cascades is the nuclear interaction length, given very roughly by

$$\lambda_I \approx 35 \text{ g cm}^{-2} A^{1/3} \ . \tag{27.30}$$

Longitudinal energy deposition profiles are characterized by a sharp peak near the first interaction point (from the fairly local deposition of EM energy resulting from π^0's produced in the first interaction), followed by a more gradual development with a maximum at

$$x/\lambda_I \equiv t_{\max} \approx 0.2 \ln(E/1 \text{ GeV}) + 0.7 \tag{27.31}$$

as measured from the front of the detector.

The depth required for containment of a fixed fraction of the energy also increases logarithmically with incident particle energy. The thickness of iron required for 95% (99%) containment of cascades induced by single hadrons is shown in Fig. 27.10 [79]. Two of the sets of data are from large neutrino experiments, while the third is from a commonly-used parameterization. Depths as measured in nuclear interaction lengths presumably scale to other materials. From the same data it can be concluded that the requirement that 95% of the energy in 95% of the showers be contained requires 40 to 50 cm (2.4 to 3.0 λ_I) more material material than for an average 95% containment. The transverse dimensions of hadronic showers also scale as λ_I, although most of the energy is contained in a narrow core.

The energy deposit in a hadronic cascade consists of a prompt EM component due to π^0 production and a somewhat slower component mainly due to low-energy hadronic activity. An induction argument verified by Monte-Carlo simulations has shown that the fraction of hadronic energy in a cascade is $(E/E_0)^{m-1}$, where $0.80 \lesssim m \lesssim 0.85$ [82]. E_0 is about 1 GeV for incident pions, and the power-law description is approximately valid for incident energy E greater than a few tens of GeV. In general, the electromagnetic and hadronic energy depositions are converted to electrical signals with different efficiencies.

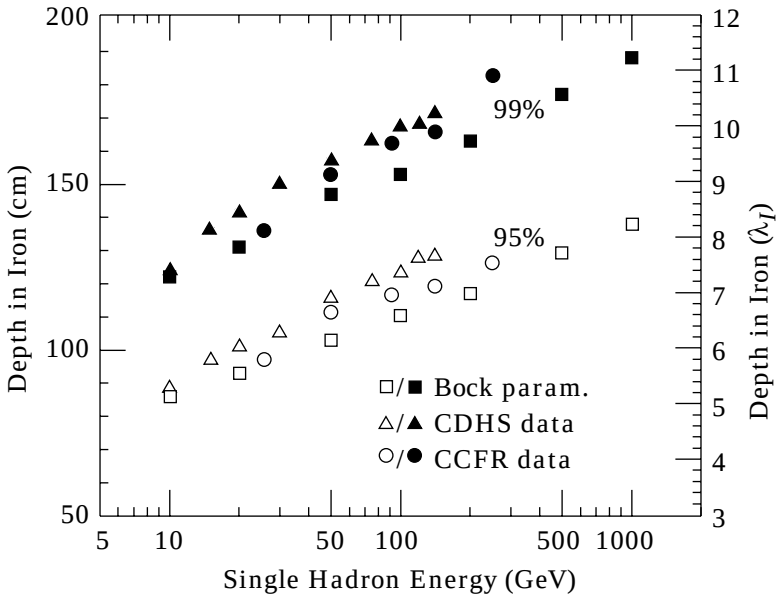

Figure 27.10: Required calorimeter thickness for 95% and 99% hadronic cascade containment in iron, on the basis of data from two large neutrino detectors and the parameterization of Bock *et al.* [79].

The ratio of the conversion efficiencies is usually called the intrinsic e/h ratio. It follows in the power-law approximation the ratio of the responses for incident pions and incident electrons is given by "π/e"$= 1 - (1 - h/e)(E/E_0)^{m-1}$. With or without the power-law approximation the response for pions is not a linear function of energy for $e/h \neq 1$. (But in any case, as the energy increases a larger and larger fraction of the energy is transferred to π^0's, and "π/e"$\rightarrow 1$.) If $e/h = 1.0$ the calorimeter is said to be *compensating*. If e/h differs from unity by more than 5% or 10%, detector performance is compromised because of fluctuations in the π^0 content of the cascades. This results in (a) a skewed signal distribution and (b) an almost-constant contribution to detector resolution which is proportional to the degree of noncompensation $|1 - h/e|$. The coefficient relating the size of the constant term to $|1 - h/e|$ is 14% according to FLUKA simulations [82], and 21% according to Wigmans' calculations [83]. (Wigmans now prefers a different approach to the "constant term" [80].)

The formula for "π/e" given above is valid for a large uniform calorimeter. Real calorimeters usually have an EM front structure which is different, and so modifications must be made in modeling the response.

In most cases e/h is greater than unity, particularly if little hydrogen is present or if the gate time is short. This is because much of the low-energy hadronic energy is "hidden" in nuclear binding energy release, low-energy spallation products, *etc.* Partial correction for these losses occurs in a sampling calorimeter with high-Z absorbers, because a disproportionate fraction of electromagnetic energy is deposited in the inactive region.

For this reason, a fully sensitive detector such as scintillator or glass cannot be made compensating.

The average electromagnetic energy fraction in a high-energy cascade is smaller for incident protons than for pions; $E_0 \approx 2.6$ GeV rather than ≈ 1 GeV. As a result "π/e">"p/e" (if $e/h > 1$) in a noncompensating calorimeter [82]. This difference has now been measured [84].

Circa 1990 compensation was thought to be very important in hadronic calorimeter design. Motivated very much by the work of Wigmans [83], several calorimeters were built with $e/h \approx 1 \pm 0.02$. These include

- ZEUS [85] 2.6 cm thick scintillator sheets sandwiched between 3.3 mm depleted uranium plates; a resolution of $0.35/\sqrt{E}$ was obtained;
- ZEUS prototype study [86], with 10 mm lead plates and 2.5 mm scintillator sheets; $0.44/\sqrt{E}$;
- D0 [87], where the sandwich cell consists of a 4–6 mm thick depleted uranium plate, 2.3 mm LAr, a G-10 signal board, and another 2.3 mm LAr gap; $45\%/\sqrt{E}$.

Approximately Gaussian signal distributions were observed.

More recently, compensation has not been considered as important, and, in addition, the new generation of calorimeters for LHC experiments operate in a different energy regime and can tolerate poorer resolution in return for simpler, deeper structures. For example, the ATLAS endcaps consist of iron plates with scintillating fiber readout [88]. The fraction of the structure consisting of low-Z active region (scintillator in this case) is much smaller than would be necessary to achieve compensation. Test beam results with these modules show a resolution of $\approx 46\%/\sqrt{E}$, and $e/h = 1.5$–1.6.

27.9.3. ***Free electron drift velocities in liquid ionization sensors***: Velocities as a function of electric field strength are given in Refs. 89–92 and are plotted in Fig. 27.11. Recent precise measurements of the free electron drift velocity in LAr have been published by W. Walkowiak [93]. These measurements were motivated by the design of the ATLAS electromagnetic calorimeter and inconsistencies in the previous literature. Velocities are systematically higher than those shown in Fig. 27.11.

27.10. Superconducting solenoids for collider detectors

Revised October 1997 by R.D. Kephart (FNAL).

27.10.1. ***Basic (approximate) equations***: In all cases SI units are assumed, so that B is in tesla, E is in joules, dimensions are in meters, and $\mu_0 = 4\pi \times 10^{-7}$.

Magnetic field: The magnetic field at the center of a solenoid of length L and radius R, having N total turns and a current I is

$$B(0,0) = \frac{\mu_0 N I}{\sqrt{L^2 + 4R^2}} \ . \tag{27.32}$$

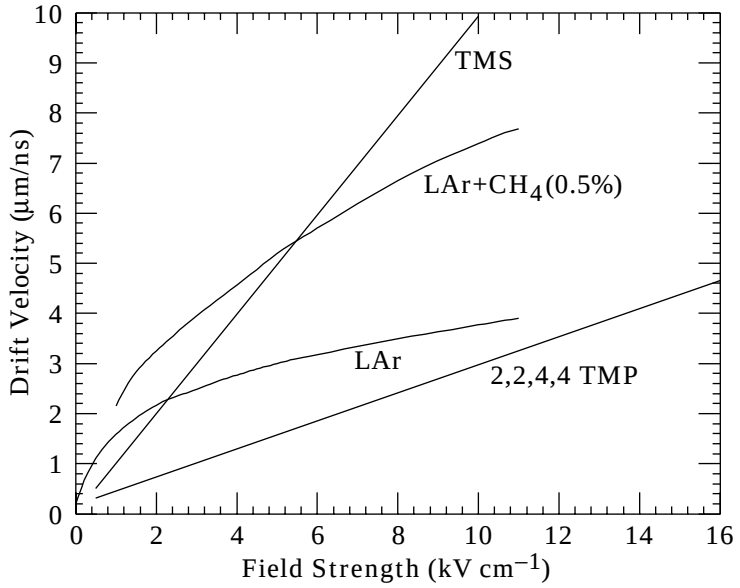

Figure 27.11: Electron drift velocity as a function of field strength for commonly used liquids.

Stored energy: The energy stored in the magnetic field of any magnet is calculated by integrating B^2 over all space:

$$E = \frac{1}{2\mu_0} \int B^2 dV \ . \tag{27.33}$$

For a solenoid with an iron flux return in which the magnetic field is $< 2T$, the field in the aperture is approximately uniform and equal to $\mu_0 NI/L$. If the thickness of the coil is small, (which is the case if it is superconducting), then

$$E \approx (\pi/2\mu_0) B^2 R^2 L \ . \tag{27.34}$$

Cost of a superconducting solenoid [94]:

$$\text{Cost (in M\$)} = 0.523 \, [E/(1 \text{ MJ})]^{0.662} \tag{27.35}$$

Magnetostatic computer programs: It is too difficult to solve the Biot-Savart equation for a magnetic circuit which includes iron components and so iterative computer programs are used. These include POISSON, TOSCA [95], and ANSYS [96].

27.10.2. ***Scaling laws for thin solenoids***: For a detector in which the calorimetry is outside the aperture of the solenoid, the coil must be thin in terms of radiation and absorption lengths. This usually means that the coil is superconducting and that the vacuum vessel encasing it is of minimum real thickness and fabricated of a material with long radiation length. There are two major contributers to the thickness of a thin solenoid:

1. The conductor, consisting of the current-carrying superconducting material (usually Cu/Nb-Ti) and the quench protecting stabilizer (usually aluminum), is wound on the inside of a structural support cylinder (usually aluminum also). This package typically represents about 60% of the total thickness in radiation lengths. The thickness scales approximately as B^2R.
2. Approximately another 25% of the thickness of the magnet comes from the outer cylindrical shell of the vacuum vessel. Since this shell is susceptible to buckling collapse, its thickness is determined by the diameter, length, and the modulus of the material of which it is fabricated. When designing this shell to a typical standard, the real thickness is

$$t = P_c D^{2.5}[(L/D) - 0.45(t/D)^{0.5}]/2.6Y^{0.4} \ , \tag{27.36}$$

where t = shell thickness (in), D = shell diameter (in), L = shell length (in), Y = modulus of elasticity (psi), and P_c = design collapse pressure (= 30 psi). For most large-diameter detector solenoids, the thickness to within a few percent is given by [97]

$$t = P_c D^{2.5}(L/D)/2.6Y^{0.4} \ . \tag{27.37}$$

27.10.3. ***Properties of collider detector solenoids***: The physical dimensions, central field, stored energy and thickness in radiation lengths normal to the beam line of the superconducting solenoids associated with the major colliders are given in Table 27.6.

The ratio of stored energy to cold mass (E/M) is a useful performance measure. One would like the cold mass to be as small as possible to minimize the thickness, but temperature rise during a quench must also be minimized. Ratios as large as 12 kJ/kg may be used. The limit is set by the maximum temperature that the coil design can tolerate during a fast quench. This maximum temperature is usually limited to < 100 K so that thermal expansion effects in the coil are manageable. This quantity is shown as a function of total stored energy for some major collider detectors in Fig. 27.12.

Table 27.6: Properties of superconducting collider detector solenoids.

Experiment–Lab	Field (T)	Bore Dia (m)	Length (m)	Energy (MJ)	Thickness (X_0)
CDF–Fermilab	1.5	2.86	5.07	30	0.86
DØ –Fermilab	2.0	1.06	2.73	5.6	0.87
BaBar–SLAC	1.5	2.80	3.46	27.0	< 1.4
Topaz–KEK*	1.2	2.72	5.4	19.5	0.70
Venus–KEK*	0.75	3.4	5.64	12	0.52
Cleo II–Cornell	1.5	2.9	3.8	25	2.5
Aleph–CERN*	1.5	5.0	7.0	130	1.7
ATLAS–CERN†	2.0	2.5	5.3	700	0.66
CMS–CERN†	4.0	5.9	12.5	2700	‡
Delphi–CERN*	1.2	5.2	7.4	109	4.0
H1–DESY	1.2	5.2	5.75	120	1.2
Zeus–DESY	1.8	1.72	2.85	10.5	0.9

*No longer in service.
†Detectors under construction.
‡EM calorimeter inside solenoid, so small X_0 not a goal.

27.11. Measurement of particle momenta in a uniform magnetic field [98,99]

The trajectory of a particle with momentum p (in GeV/c) and charge ze in a constant magnetic field $\overrightarrow{B}$ is a helix, with radius of curvature R and pitch angle λ. The radius of curvature and momentum component perpendicular to $\overrightarrow{B}$ are related by

$$p \cos\lambda = 0.3\, z\, B\, R \ , \tag{27.38}$$

where B is in tesla and R is in meters.

The distribution of measurements of the curvature $k \equiv 1/R$ is approximately Gaussian. The curvature error for a large number of uniformly spaced measurements on the trajectory of a charged particle in a uniform magnetic field can be approximated by

$$(\delta k)^2 = (\delta k_{\rm res})^2 + (\delta k_{\rm ms})^2 \ , \tag{27.39}$$

where $\delta k =$ curvature error
$\delta k_{\rm res} =$ curvature error due to finite measurement resolution
$\delta k_{\rm ms} =$ curvature error due to multiple scattering.

If many (≥ 10) uniformly spaced position measurements are made along a trajectory in a uniform medium,

$$\delta k_{\rm res} = \frac{\epsilon}{L'^2}\sqrt{\frac{720}{N+4}} \ , \tag{27.40}$$

where $N =$ number of points measured along track
$L' =$ the projected length of the track onto the bending plane
$\epsilon =$ measurement error for each point, perpendicular to the trajectory.

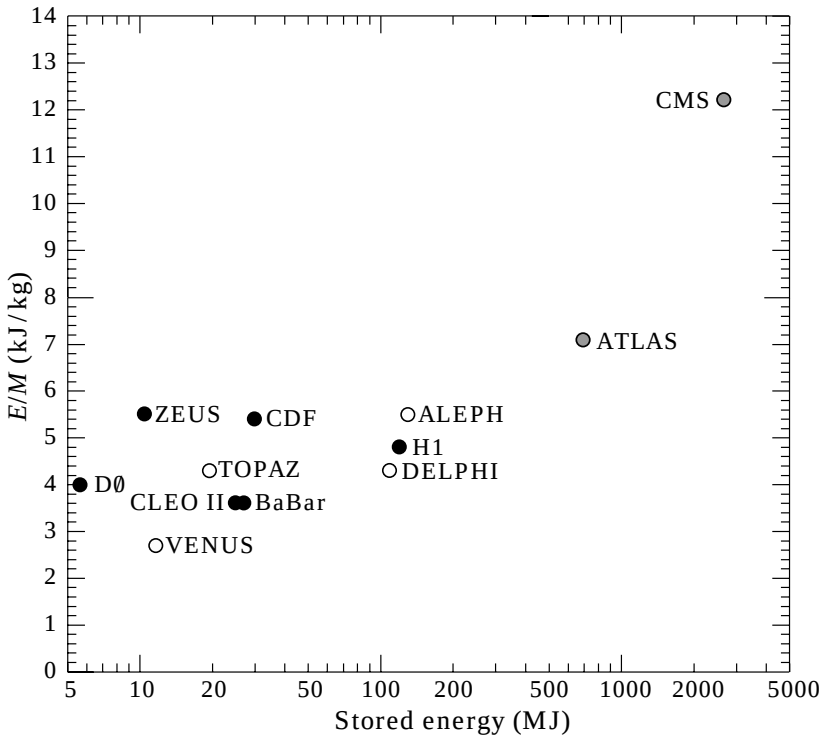

Figure 27.12: Ratio of stored energy to cold mass for existing thin detector solenoids. Solenoids in decommissioned detectors are indicated by open circles. Solenoids for detectors under construction are indicated by grey circles.

If a vertex constraint is applied at the origin of the track, the coefficient under the radical becomes 320.

For arbitrary spacing of coordinates s_i measured along the projected trajectory and with variable measurement errors ϵ_i the curvature error $\delta k_{\rm res}$ is calculated from:

$$(\delta k_{\rm res})^2 = \frac{4}{w} \; \frac{V_{ss}}{V_{ss}V_{s^2s^2} - (V_{ss^2})^2} \; , \tag{27.41}$$

where V are covariances defined as $V_{s^m s^n} = \langle s^m s^n \rangle - \langle s^m \rangle \langle s^n \rangle$ with $\langle s^m \rangle = w^{-1} \sum ({s_i}^m / {\epsilon_i}^2)$ and $w = \sum {\epsilon_i}^{-2}$.

The contribution due to multiple Coulomb scattering is approximately

$$\delta k_{\rm ms} \approx \frac{(0.016)({\rm GeV}/c)z}{Lp\beta\cos^2\lambda} \sqrt{\frac{L}{X_0}} \; , \tag{27.42}$$

where $p =$ momentum (GeV/c)
$z =$ charge of incident particle in units of e

$L =$ the total track length

$X_0 =$ radiation length of the scattering medium (in units of length; the X_0 defined elsewhere must be multiplied by density)

$\beta =$ the kinematic variable v/c.

More accurate approximations for multiple scattering may be found in the section on Passage of Particles Through Matter (Sec. 26 of this *Review*). The contribution to the curvature error is given approximately by $\delta k_{\rm ms} \approx 8 s^{\rm rms}_{\rm plane}/L^2$, where $s^{\rm rms}_{\rm plane}$ is defined there.

References:

1. *Experimental Techniques in High Energy Physics*, T. Ferbel (ed.) (Addison-Wesley, Menlo Park, CA, 1987).
2. J.B. Birks, The Theory and Practice of Scintillation Counting (Pergamon, London, 1964).
3. D. Clark, Nucl. Instrum. Methods **117**, 295 (1974).
4. J.B. Birks, Proc. Phys. Soc. **A64**, 874 (1951).
5. B. Bengston and M. Moszynski, Nucl. Instrum. Methods **117**, 227 (1974);
   J. Bialkowski *et al.*, Nucl. Instrum. Methods **117**, 221 (1974).
6. *Proceedings of the Symposium on Detector Research and Development for the Superconducting Supercollider*, eds. T. Dombeck, V. Kelly, and G.P. Yost (World Scientific, Singapor, 1991).
7. I.B. Berlman, Handbook of Fluorescence Spectra of Aromatic Molecules, 2nd edition (Academic Press, New York, 1971).
8. C. Zorn in Instrumentation in High Energy Physics, ed. F. Sauli, (1992, World Scientific, Singapore) pp. 218–279.
9. T. Foerster, Ann. Phys. **2**, 55 (1948).
10. J.B. Birks, The Theory and Practice of Scintillation Counting, Chapter 6, (Pergamon, London, 1964);
    J.M. Fluornoy, Conference on Radiation-Tolerant Plastic Scintillators and Detectors, K.F. Johnson and R.L. Clough editors, Rad. Phys. and Chem., **41** 389 (1993).
11. D. Horstman and U. Holm, *ibid,* 395.
12. D. Blomker *et al.*, Nucl. Instrum. Methods **A311**, 505 (1992);
    J. Mainusch *et al.*, Nucl. Instrum. Methods **A312**, 451 (1992).
13. Conference on Radiation-Tolerant Plastic Scintillatora and Detectors, K.F. Johnson and R.L. Clough editors, Rad. Phys. and Chem., **41** (1993).
14. S.R. Borenstein and R.C. Strand, IEEE Trans. Nuc. Sci. **NS-31(1)**, 396 (1984).
15. P. Sonderegger, Nucl. Instrum. Methods **A257**, 523 (1987).
16. S.A. Sedykh *et al.*, Nucl. Instrum. Methods **A455**, 346 (2000).
17. SCIFI 97: Conference on Scintillating Fiber Detectors, 1997 University of Notre Dame, Indiana, eds. A. Bross, R. Ruchti, and M. Wayne.
18. K.F. Johnson, Nucl. Instrum. Methods **A344**, 432 (1994).

19. C.M. Hawkes *et al.*, Nucl. Instrum. Methods **A292**, 329 (1990).
20. R.K. Swank, Ann. Rev. Nucl. Sci. **4**, 137 (1954);
    G.T. Wright, Proc. Phys. Soc. **B68**, 929 (1955).
21. M. Laval *et al.*, Nucl. Instrum. Methods **206**, 169 (1983).
22. M. Moszynski *et al.*, Nucl. Instrum. Methods **A226**, 534 (1984).
23. E. Blucher *et al.*, Nucl. Instrum. Methods **A249**, 201 (1986).
24. C. Bebek, Nucl. Instrum. Methods **A265**, 258 (1988).
25. S. Kubota *et al.*, Nucl. Instrum. Methods **A268**, 275 (1988).
26. B. Adeva *et al.*, Nucl. Instrum. Methods **A289**, 35 (1990).
27. I. Holl, E. Lorentz, G Mageras, IEEE Trans. Nucl. Sci. **35**, 105 (1988).
28. J. Litt and R. Meunier, Ann. Rev. Nucl. Sci. **23**, 1 (1973).
29. D. Bartlett *et al.*, Nucl. Instrum. Methods **A260**, 55 (1987).
30. P. Duteil *et al.*, Review of Scientific Instruments **35**, 1523 (1964).
31. M. Cavalli-Sforza *et al.*, Construction and Testing of the SLC Čerenkov Ring Imaging Detector, IEEE **37**, N3:1132 (1990).
32. E.G. Anassontzis *et al.*, Recent Results from the DELPHI Barrel Ring Imaging Cherenkov Counter, IEEE **38**, N2:417 (1991).
33. R.T. Rewick *et al.*, Anal Chem 60, 2095 (1989).
34. B. Dolgoshein, "Transition Radiation Detectors," Nucl. Instrum. Methods **A326**, 434 (1993).
35. X. Artru *et al.*, Phys. Rev. **D12**, 1289 (1975).
36. G.M. Garibian *et al.*, Nucl. Instrum. Methods **125**, 133 (1975).
37. RD6 Collaboration, CERN/DRDC 90-38 (1990); CERN/DRDC 91-47 (1991); CERN/DRDC 93-46 (1993).
38. ATLAS Collaboration, ATLAS Inner Detector Technical Design Report, Volume 2, ATLAS TDR 5, CERN/LHCC/97-16 (30 April 1997).
39. B. Dolgoshein, Nucl. Instrum. Methods **252**, 137 (1986).
40. C.W. Fabjan *et al.*, Nucl. Instrum. Methods **185**, 119 (1981).
41. J. Cobb *et al.*, Nucl. Instrum. Methods **140**, 413 (1977).
42. A. Büngener *et al.*, Nucl. Instrum. Methods **214**, 261 (1983).
43. R.D. Appuhn *et al.*, Nucl. Instrum. Methods **263**, 309 (1988).
44. Y. Watase *et al.*, Nucl. Instrum. Methods **248**, 379 (1986).
45. R. Ansari *et al.*, Nucl. Instrum. Methods **263**, 51 (1988).
46. H.J. Butt *et al.*, Nucl. Instrum. Methods **252**, 483 (1986).
47. J.F. Detoeuf *et al.*, Nucl. Instrum. Methods **265**, 157 (1988).
48. M. Holder *et al.*, Nucl. Instrum. Methods **263**, 319 (1988).
49. H. Weidkamp, DiplomArbeit, Rhein-Westf. Tech. Hochschule Aachen (1984).
50. H. Grässler *et al.*, Proc. Vienna Wire Chamber Conference (1989).

51. T. Akesson *et al.*, CERN Preprint, CERN-PPE/97-161 (1997), to be published in Nucl. Instr. and Meth.
52. F.F. Rieke and W. Prepejchal, Phys. Rev. **A6**, 1507 (1972).
53. L.G. Christophorou, "Atomic and molecular radiation physics" (Wiley, London 1991).
54. G. Charpak *et al.*, Nucl. Instrum. Methods **62**, 262 (1968).
55. R. Veenhof, GARFIELD program: simulation of gaseous detectors, version 6.32, CERN Program Library Pool W999 (W5050).
56. As representative examples see: B. Adeva *et al.*, Nucl. Instrum. Methods **A287**, 35 (1990).
57. As representative example see: A. Alexander *et al.*, Nucl. Instrum. Methods **A276**, 42 (1989).
58. As representative examples see: F. Bedeschi *et al.*, Nucl. Instrum. Methods **A268**, 50 (1988);
    Opal Collaboration: Nucl. Instrum. Methods **A305**, 275 (1991).
59. A. Oed, Nucl. Instrum. Methods **A263**, 351 (1988).
60. W. Blum and L. Rolandi, *Particle Detection with Drift Chambers*, Springer-Verlag (1994).
61. A. Peisert and F. Sauli, CERN-84-08 (Jul 1984).
62. R. Bellazzini and A. M. Spezziga, Rivista del Nuovo Cimento **17**, 1 (1994).
63. D.R. Nygren and J.N. Marx, "The Time Projection Chamber," Phys. Today **31**, 46 (1978).
64. P. Weilhammer, Nucl. Instrum. Methods **A453**, 60 (2000).
65. G. Lindström *et al.*, Nucl. Instrum. Methods **A465**, 60 (2001).
66. G. Lindström *et al.*, Nucl. Instrum. Methods **A426**, 1 (1999).
67. V. Radeka, IEEE Trans. Nucl. Sci. **NS-15/3**, 455 (1968);
    V. Radeka, IEEE Trans. Nucl. Sci. **NS-21**, 51 (1974).
68. F.S. Goulding, Nucl. Instrum. Methods **100**, 493 (1972);
    F.S. Goulding and D.A. Landis, IEEE Trans. Nucl. Sci. **NS-29**, 1125 (1982).
69. H. Spieler, IEEE Trans. Nucl. Sci. **NS-29**, 1142 (1982).
70. W.R. Nelson, H. Hirayama and D.W.O. Rogers, "The EGS4 Code System," SLAC-265, Stanford Linear Accelerator Center (Dec. 1985).
71. D. Hitlin *et al.*, Nucl. Instrum. Methods **137**, 225 (1976). See also W. J. Willis and V. Radeka, Nucl. Instrum. Methods **120**, 221 (1974), for a more detailed discussion.
72. E. Bloom and C. Peck, Ann. Rev. Nucl. and Part. Sci. **33**, 143 (1983).
73. M.A. Akrawy *et al.*, Nucl. Instrum. Methods **A290**, 76 (1990).
74. H. Burkhardt *et al.*, Nucl. Instrum. Methods **A268**, 116 (1988).
75. W. Hoffman *et al.*, Nucl. Instrum. Methods **163**, 77 (1979).

76. M.A. Schneegans *et al.*, Nucl. Instrum. Methods **193**, 445 (1982).
77. C. Fabjan and R. Wigmans, Rept. Prog. Phys. **52**, 1519 (1989).
78. J.V. Allaby *et al.*, Nucl. Instrum. Methods **A281**, 291 (1989).
79. D. Bintinger, in *Proceedings of the Workshop on Calorimetry for the Supercollider*, Tuscaloosa, AL, March 13–17, 1989, edited by R. Donaldson and M.G.D. Gilchriese (World Scientific, Teaneck, NJ, 1989), p. 91;
    R.K. Bock, T. Hansl-Kozanecka, and T.P. Shah, Nucl. Instrum. Methods **186**, 533 (1981).
80. R. Wigmans, *Calorimetry: Energy Measurment in Particle Physics*, Clarendon, Oxford (2000).
81. C. Leroy and P.-G. Rancoita, Rep. Prog. Phys. **63**, 505 (2000).
82. T.A. Gabriel, D.E. Groom, P.K. Job, N.V. Mokhov, and G.R. Stevenson, Nucl. Instrum. Methods **A338**, 336 (1994).
83. R. Wigmans, Nucl. Instrum. Methods **A259**, 389 (1987);
    R. Wigmans, Nucl. Instrum. Methods **A265**, 273 (1988).
84. N. Akchurian *et al.*, Nucl. Instrum. Methods **A408**, 380 (1998).
85. U. Behrens *et al.*, Nucl. Instrum. Methods **A289**, 115 (1990);
    A. Bernstein *et al.*, Nucl. Instrum. Methods **A336**, 23 (1993).
86. E. Bernardi *et al.*, Nucl. Instrum. Methods **A262**, 229 (1987).
87. S. Abachi *et al.*, Nucl. Instrum. Methods **A324**, 53 (1993).
88. F. Ariztizabal *et al.*, Nucl. Instrum. Methods **A349**, 384 (1994).
89. E. Shibamura *et al.*, Nucl. Instrum. Methods **131**, 249 (1975).
90. T.G. Ryan and G.R. Freeman, J. Chem. Phys. **68**, 5144 (1978).
91. W.F. Schmidt, "Electron Migration in Liquids and Gases," HMI B156 (1974).
92. A.O. Allen, "Drift Mobilities and Conduction Band Energies of Excess Electrons in Dielectric Liquids," NSRDS-NBS-58 (1976).
93. W. Walkowiak, Nucl. Instrum. Methods **A449**, 288 (2000).
94. M.A. Green, R.A. Byrns, and S.J. St. Lorant, "Estimating the cost of superconducting magnets and the refrigerators needed to keep them cold," in *Advances in Cryogenic Engineering*, Vol. 37, Plenum Press, New York (1992).
95. Vector Fields, Inc., 1700 N. Farnsworth Ave., Aurora, IL.
96. Swanson Analysis Systems, Inc., P.O. Box 65, Johnson Rd., Houston, PA.
97. CGA-341-1987, "Standard for insulated cargo tank specification for cryogenic liquids," Compressed Gas Association, Inc., Arlington, VA (1987).
98. R.L. Gluckstern, Nucl. Instrum. Methods **24**, 381 (1963).
99. V. Karimäki, Nucl. Instrum. Methods **A410**, 284 (1998).